Interfacial engineering of oxygenated chemical bath-deposited CdS window layer for highly efficient Sb_2Se_3 thin-film solar cells

Liping Guo[a,1], Baiyu Zhang[b,1], Shan Li[c], Lin Li[a], Guozhong Xing[d], Qian Zhang[c*], Xiaofeng Qian[b**] and Feng Yan[a,e***]

[a]Department of Metallurgical and Materials Engineering, The University of Alabama, Tuscaloosa, Alabama, 35487, USA
[b]Department of Materials Science and Engineering, College of Engineering and College of Science, Texas A&M University, College Station, Texas 77843, USA
[c]Department of Materials Science and Engineering, Harbin University of Technology, Shenzhen, 518055, China.
[d]United Microelect Corp. Ltd., 3 Pasir Ris Dr 12, Singapore 519528, Singapore
[e]Center for Materials in Information Technology, The University of Alabama, Tuscaloosa, AL, 35487

[1]These authors contribute equally to the paper.

Antimony chalcogenides with one-dimensional ribbon structures represent a new group of cost-effective, nontoxic and earth-abundant photovoltaics. In this work, interfacial engineering of oxygenated chemical bath deposited (CBD) CdS buffer layers were used to tailor Sb_2Se_3 thin film solar cells deposited using the closed spaced sublimation (CSS) deposition process. Sb_2Se_3 solar cells with oxygenated CBD CdS have demonstrated a champion power conversion efficiency (PCE) of 6.3% with graphite as the back contact. Van der Waals (vdW) gap in Sb_2Se_3 is regulated via oxygen diffusion, which significantly influences the growth direction of $(Sb_4Se_6)_n$ quasi-one-dimensional nanoribbons. The improved interface quality and ribbon orientation, in turn, enhance the electrical and optical properties as well as device performance of the Sb_2Se_3 solar cells. The defects level and corresponding devices performance associated with the oxygen environmental were characterized in both theoretical and experimental approaches. This work provides an effective way to tune the microstructure and electronic structures of non-cubic chalcogenides by tailoring the interfacial area of the window layer and inner vdW gaps of Sb_2Se_3 solar cells.

* corresponding author email: zhangqf@hit.edu.cn
** corresponding author email: feng@tamu.edu
*** corresponding author email: fyan@eng.ua.edu

Keywords: Sb_2Se_3 thin film solar cell, Chemical bath deposition, Close space sublimation, oxygenated, CdS window layer

1. Introduction

Solar cells, directly converting solar energy into electricity, provide renewable, sustainable, and affordable energy.[1-3] Antimony selenide, Sb_2Se_3, is considered as a promising absorber material for solar cells due to its suitable bandgap (~1.2 eV direct bandgap and 1.1 eV indirect bandgap, respectively), high absorption coefficient (~10^5 cm^{-1}), abundant natural source as well as low-toxicity compared to conventional CdTe and GaAs[4-6]. To date, the Sb_2Se_3 solar cells have been widely investigated using several grown techniques, such as chemical bath deposition (CBD), rapid thermal evaporation (RTE), vapor transport deposition (VTD), and close space sublimation (CSS), yielding the highest PCE around ~9%, although the PCE is still low compared to record CdTe and CuInGaSe (CIGS) solar cells with PCE of ~22%.[6-13] To improve the PCE of Sb_2Se_3 solar cells, considerable strategies have been explored, including tuning the $(Sb_4Se_6)_n$ ribbons orientation with buffer layer structure for Sb_2Se_3, such as CdS, ZnO, TiO_2.[5, 6, 14, 15] Selenium compensation (*i.e.,* selenization) into the as-deposited Sb_2Se_3 suppress the Se vacancies and improves the device performance.[16] Although CdS is toxic, it is the most commonly used window layer in CdTe solar cell due to its desired bandgap (~ 2.4 eV), small lattice mismatch, and *n*-type electronic behavior for the large-scale manufacturing. However, the CdS with a bandgap of 2.4 eV will absorb the blue light (photon energy > 2.4 eV) and limit the photocurrent in the solar cells.[17, 18] To address this problem, reducing the CdS thickness is an effective approach to improve the light transmittance in the CdS window layer.[19] Nevertheless, thinner buffer layers may degrade open circuit voltage and fill factor due to increased pinhole concentration.[20, 21]

For the Sb_2Se_3 solar cells with a CdS buffer layer, the Cd diffusion could decrease the *p*-type conductivity of Sb_2Se_3 because the Cd^{2+} ions occupy the Sb^{3+} site.[22] On the other hand, a small bandgap window layer can effectively improve the photocurrent via varying the device spectral response [23, 24]. For example, CdSe as a window layer for CdTe could improve the photocurrent because the reduced absorber bandgap can absorb more light due to interdiffusion between CdTe and CdSe although CdSe is intrinsically a worse windows layer for CdTe.[24] Post-annealing of chemical bath deposited (CBD) CdS layer in the air can also reduce the bandgap of the CdS layer due to the recrystallization, sulfur evaporation and self-oxidation of the CdS films.[25] In addition, oxygen in the ZnO and ambient $CdCl_2$ treated CdS buffer layers for Sb_2Se_3 solar cells could significantly impact the device performance by tuning the oxygen concentration in the buffer layer, and even the oxygen introduced into the Sb_2Se_3 during film deposition could improve the efficiency due to passivation of interfacial defect states between CdS/Sb_2Se_3.[26] These oxygen associated observations indicate that the oxygen in the buffer layer and absorbers plays a critical role in the Sb_2Se_3 device performance. However, it is still not clear how the oxygen impact on the Sb_2Se_3 device performance fundamentally. Particularly, how the oxygen existing in the atomistic level contributes to the solar cells power conversion efficiency (PCE).

In this work, we utilize the first-principles theoretical calculations to elucidate the role of oxygen in the interface between the CdS buffer layer and Sb_2Se_3 absorber layer and succeed experimentally in improving the device performance with the theoretical prediction. The oxygen associated defects and intrinsic defects, the microstructure variation, electronic behaviors, and oxygen diffusion mechanism in Sb_2Se_3 has been systematically studied. It is demonstrated that oxygen associated defects in Sb_2Se_3 are benign defects. In addition, the enhanced device performance of Sb_2Se_3 thin film solar cells with oxygenated CdS buffer layer can be associated

with the isotropic oxygen diffusion into the Sb_2Se_3 to form an Sb-O-Se chain, filled the van der Waals (vdWs) gap among the quasi-one-dimensional ribbons. We experimentally demonstrate that oxygenated chemical bath deposited (CBD) CdS could improve the photocurrent and voltage and boost the Sb_2Se_3 PCE to 6.3%. The improved interfacial quality and oxygen diffusion between oxygenated CBD CdS:O buffers and Sb_2Se_3 absorber can benefit the solar cells device performance. In addition, the oxygen diffusion from the oxygenated CBD CdS could tailor the $(Sb_4Se_6)_n$ ribbon orientation. This provides a unique pathway to engineering the ribbon orientation dependent electronic and photonic behavior and heterojunction interface recombination in Sb_2Se_3 like non-cubic chalcogenide photovoltaics.

2. Experimental Details.

2.1 First Principle Calculation

Atomistic, electronic structures, and defect formation energy were calculated using first-principles density functional theory (DFT)[27] as implemented in the Vienna Ab initio Simulation Package (VASP)[28]. The Perdew-Burke-Ernzerhof (PBE)[29] form of exchange-correlation functional within the generalized gradient approximation (GGA)[30] and a plane wave basis set with a 400eV energy cutoff were employed for VASP calculations. Since van der Waals interaction is present between neighboring $(Sb_4Se_6)_n$ ribbons, we adopted optB86-vdW non-local correlation functional that approximately accounts for dispersion interactions[31]. The structural optimization and electronic relaxation were calculated using a Γ-centered Monkhorst-Pack[32] k-point sampling grid of 12×4×4. The maximal residual force of each atom is less than 0.02 eV $Å^{-1}$ and the convergence criteria for electronic relaxation was set to 10^{-6} eV. As the DFT-GGA often underestimates the band gap, we adopt the modified Becke-Johnson (MBJ) exchange potential[33] and hybrid HSE06 functional[34] for electronic structure and optical property calculations, and a

k-point grid of 28×12×12 used in the MBJ calculations, and a k-point grid of 9 × 3 × 3 used in the HSE06 calculations. The MBJ calculation yields a band gap close to that from the HSE06 calculation for Sb_2Se_3. The charge defect formation energy, the chemical potential energy calculation can be found in the supporting information.

2.2 Materials and Solar cells fabrication

CdS films (~60-80 nm thickness) were fabricated through chemical bath deposition on the F doped SnO_2 coated soda lime glass (FTO, Pilkington NSG TEC 15). FTO substrates were cleaned with Hellmanex 2% solution, Acetone, isopropyl alcohol, and deionized water cleaned in an ultrasonic bath. $CdSO_4$ and Thiourea solution were used as raw materials to form reaction solutions with NH_4OH added in to tune the PH value. The whole reaction took place in a chemical bath with a constant temperature of 70 ^oC for about 10 minutes. Then the CdS coated FTOs are taken out and cleaned in deionized water to remove the loose particles. The as-deposited CdS films were annealed under various oxygen conditions in a rapid thermal process (RTP) with oxygen partial pressure control. The ratio of O_2/O_2+Ar was tuned to be 0%, 21%, 62%, and 92%, respectively, by turning the mixture gas flows connected to argon and oxygen gas. All annealing processes were under a temperature of 400^{o}C for 10min. Sb_2Se_3 films were grown by close-spaced sublimation (CSS) with the pure Sb_2Se_3 powders (99.999%, Alfa Aesar) as reported previously [35]. The CdS:O doped substrate-source distance was about 8 mm. The substrate temperature was set at 300 ^oC, and the source temperature was 550 ^oC. The base pressure was about 5 mTorr with Ar gas purge before the deposition. The deposited Sb_2Se_3 film was about 800 nm in thickness. Sb_2Se_3 thin film solar cells were fabricated with conventional superstrate device structure: glass/FTO/CdS:O/Sb_2Se_3/Graphite/Ag. Graphite back contact was screen-printed followed by Ag slurry. Each device had a total area of approximately 0.08 cm^2 defined by the mask pattern.

2.3 *Materials and Solar Cells Characterization*

The structure of CdS:O and Sb_2Se_3 film were characterized by X-Ray Diffraction (XRD) with Cu Kα radiation (X'Pert). Raman experiments were conducted on a single stage Raman spectrometer with a solid-state laser (Horiba LabRam HR, 532 nm wavelength). Morphology of CdS:O was investigated by Atomic Force Microscopy (AFM, Park XE70). The absorbance and transmittance spectra were measured using a UV-Vis spectrometer (Shimadzu UV-1800). X-Ray photoelectron spectroscopy was collected using the Kratos Axis 165 XPS with Al source. The thickness and the elemental distribution were characterized using the scanning electron microscopy (SEM, JEOL 7000) equipped with Energy dispersive X-ray spectroscopy (EDX). Current density-voltage (*J-V*) characteristics were measured by the Newport Sol3A class AAA solar simulator (Oriel, model 94023A, Newport Corporation, Irvine, CA, USA) under ambient conditions (room temperature, 1000W/m, air mass (AM) 1.5 G illumination). A Keithley 2420 source meter (Keithley Instrument Inc.) was used to acquire *J-V* characteristics. External Quantum efficiency (EQE) of solar cells was measured with a solar cell spectral response measurement system (QE-T, Enli Technology, Co. Ltd).

3. Results and discussion

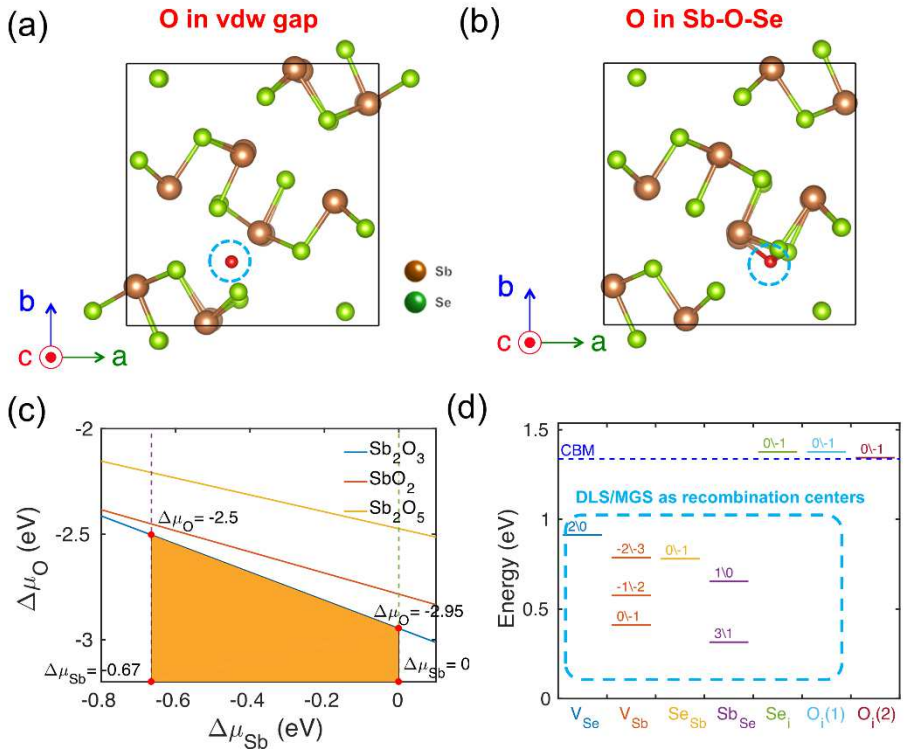

Fig. 1. (a) and (b) Two possible Sb_2Se_3:O configurations: (a) O in the van der Waals (vdWs) gap, and (b) Sb-O-Se chain formation. (c) The allowed chemical potential of species. (d) Charged defect transition levels.

To understand the effect of oxygen doping on Sb_2Se_3 device performance, we first conduct first-principles density functional theory (DFT) calculations[27, 36] and investigate the oxygen associated fundamental structural and electronic properties. To mimic the dilute limit of impurities, we employ a 1× 1× 3 supercell of Sb_2Se_3. After relaxing a series of structures wherein the oxygen atom stays in a variety of potential interstitial sites, oxygen atoms can be stabilized by either locating at van der Waals (vdWs) gaps (Fig.1a) or bonding with Sb and Se atoms within the same ribbon (*i.e.*, forming the Sb-O-Se chain, shown in Fig. 1b). The defect tolerance of solar cell absorbers is of great importance to the device performance, where the Se rich and Se poor conditions could be used to tailor the defects and optimized the carrier transport behavior.[37] The intrinsic defect formation energy can be tuned by chemical potentials of host cell elements, while

the formation energy of oxygen-induced point defects (*i.e.* O_i, interstitial defect) is also dependent on the chemical potential of O. Figure 1(c) shows that the region of oxygen chemical potential where the formation of antimony oxides is forbidden. Chemical potentials of each element are associated with synthesis conditions. It's noteworthy that O substitution (O_{Se}) defect requires relatively low energy, indicating the possibility of oxygen occupying Se vacancy site after doping. However, Se vacancy will introduce defect localized state (DLS) as shown in Fig. 1(f), which acts as carrier recombination centers. Figure 1(f) also shows that oxygen interstitials are benign defects and will not introduce any mid-gap state. On the other hand, the doped O atoms may saturate at Se vacancy sites, eliminating the DLS caused by the absence of Se atoms. Our band structure calculations shown in Figure S1 further confirm the transition level diagram where a flat band appears in the middle of the band gap in the host cell with Se vacancy. After adding one oxygen to Se site (i.e., O_{Se}, substitution defects), the band gap becomes clean. In addition, the band structures of the crystal with O interstitials do not possess any bands within the band gap, indicating the absence of DLSs. Thus, our DFT-based defect study suggests that oxygen associated defects in the Sb_2Se_3 absorber will not degrade the solar cell device, and may even benefit the performance of Sb_2Se_3 absorber layer.

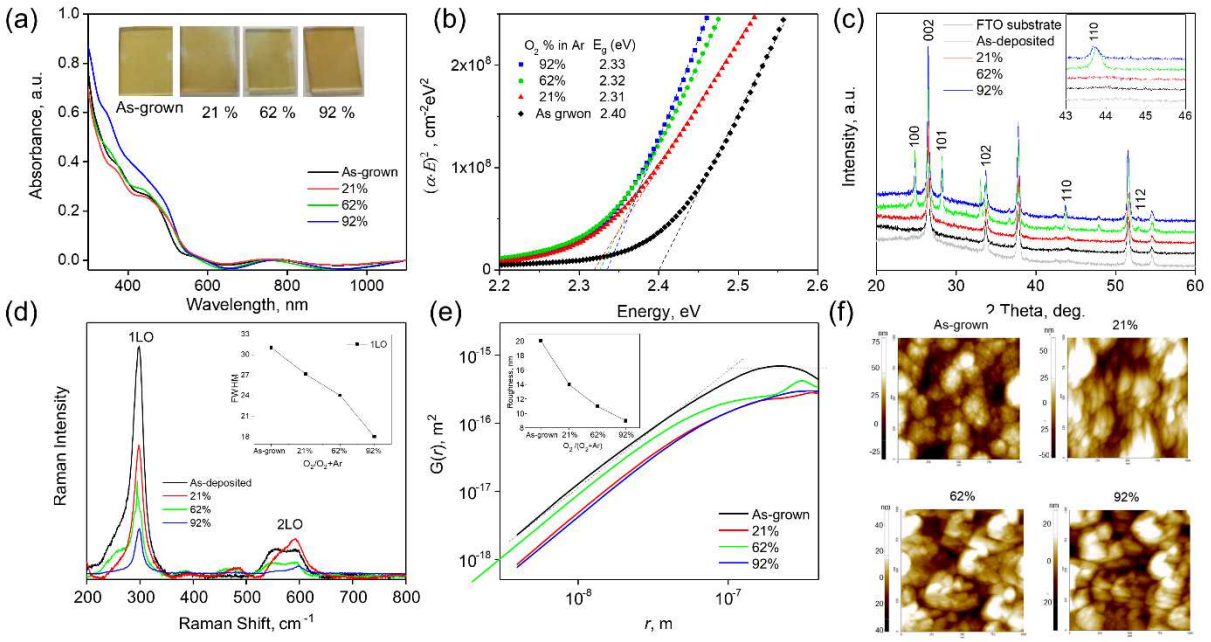

Fig. 2. Characterization of the oxygenated CBD CdS thin films treated under various oxygen partial pressure: (a) Absorbance with inset of optical images of the treated films, (b) bandgap determined by the Tauc plots, (c) X-ray spectra, (d) Raman spectra, (e) height profiles of the AFM images, 1×1 □m^2, and (f) Atomic force microscopy (AFM) images.

To validate about our calculation results, we first systematically investigated the influences of the oxygen concentration in the CBD grown CdS thin film (~ 60 nm thickness) by tuning the annealing oxygen concentration to gradually introduce oxygen to the following Sb_2Se_3 through interface diffusion. The optical response was characterized using UV-Vis spectra, as shown in Fig. 2. The CdS films were annealed in 21%, 62%, and 92% oxygen partial pressure, i.e., $O_2/(O_2+Ar)$ at 400 ^oC for 10 mins. The absorbances of the oxygenated CBD CdS films are shown in Fig.2a, where oxygenated CdS shows higher absorption in the blue range (<500 nm, red-shift in absorption edge). Meanwhile, the color of these films changes from yellow to brownish-yellow, as shown in the inset of Fig. 2a, suggesting that the reduced bandgap of CdS film oxidation occurs in the presentence of oxygen [25]. This is opposite to the sputtered CdS in oxygen partial pressure with increased bandgap due to wide bandgap CdSOx formation[20]. The bandgap of these oxygenated

CdS was determined as shown in Fig. 2b, where the bandgap of the films changes from 2.4 eV to 2.3 eV. When the oxygen partial pressure is less than 21%, the bandgap reduces from 2.4 to 2.31 eV due to the oxygen incorporation and CdO formation with a bandgap of ~ 1.6 eV[38]. With increasing the oxygen partial pressure more than 21%, the bandgap slight increases, potentially due to a mixture of CdS, $CdSO_3$ and $CdSO_4$ [20, 39], as shown in Figure S2 (see in the supporting information).

The structural properties of these oxygenated CBD CdS films were characterized using the X-ray diffraction (XRD, Fig.2c). The hexagonal wurtzite structures are indexed in the figure. The XRD indicates that the crystallization is improved by introducing more oxygen. In particular, the as-deposited film annealed at lower oxygen partial pressure (< 21%) displays weak intensity, while peak intensity increases with increasing the oxygen partial pressure, suggesting that the as-grown film exhibits nanocrystalline behavior and higher oxygen concentration improves crystallinity. In addition, the peaks at high angle (i.e., (110) peak shown in the inset of Fig. 2a) shift towards low angle at higher oxygen content, indicating slightly enlarged lattice constants of oxygenated CdS films caused by potential oxygen interstitials. Raman spectra were collected for these oxygenated CBD CdS, as shown in Fig. 2d. The longitudinal optical (LO) phonon (crystal mode) in the oxygenated CBD CdS was analyzed. The Raman intensities decrease with increased oxygen partial pressure, and the asymmetric broadening to the lower frequency can be associated with the phonon confinement effect due to the structure fluctuation[40]. However, the spectra width measured by the full width at half maximum (FWHM), as shown in the inset of Fig. 2b decreases compared to the as-grown one. It could be ascribed to that the surface oxygen on the CBD CdS [25]. Thus, the decreased bandgap (red-shift) could be directly linked to the lattice dilatation due to the interstitial oxygen with the bond stretching between Cd-S (CdS:O). With the introduction of more oxygen

into CdS, the slightly increased bandgap (blue-shift) could be explained as the formation of $CdSO_x$ (at higher phonon frequency, 2 LO).

To estimate the surface quality of the oxygenated CBD CdS films, atomic force microscopy (AFM) was employed to characterize the morphology of the CdS films. Figure 2e shows the AFM topography of CdS films oxygenated at various oxygen partial pressure. The typical polycrystalline thin films have been observed under different oxygen partial pressure. The root-mean-square (RMS) roughness is significantly reduced, as shown in the inset of Fig. 2e, suggesting that the smoothening of CdS thin film is effective with the introduction of more oxygen into the CdS surface. The growth dynamics assessed from the height-height correlation function (HHCF) *G*(r) is defined as $G(r) = \langle [h(\overrightarrow{r_2})] - [h(\overrightarrow{r_1})] \rangle$ for each film, as shown in Fig. 2f. The curves are down-shifted as oxygen partial pressure increases. It suggests that the smoothening of the oxygenated CdS could result from the oxygen on the surface diffusion towards the regions with lower surface energy (e.g., boundaries) at nanoscale[41, 42]. This also indicates that the CdS:O/Sb_2Se_3 interface quality can be improved, which may benefit the electronic and optical properties of the solar cells.

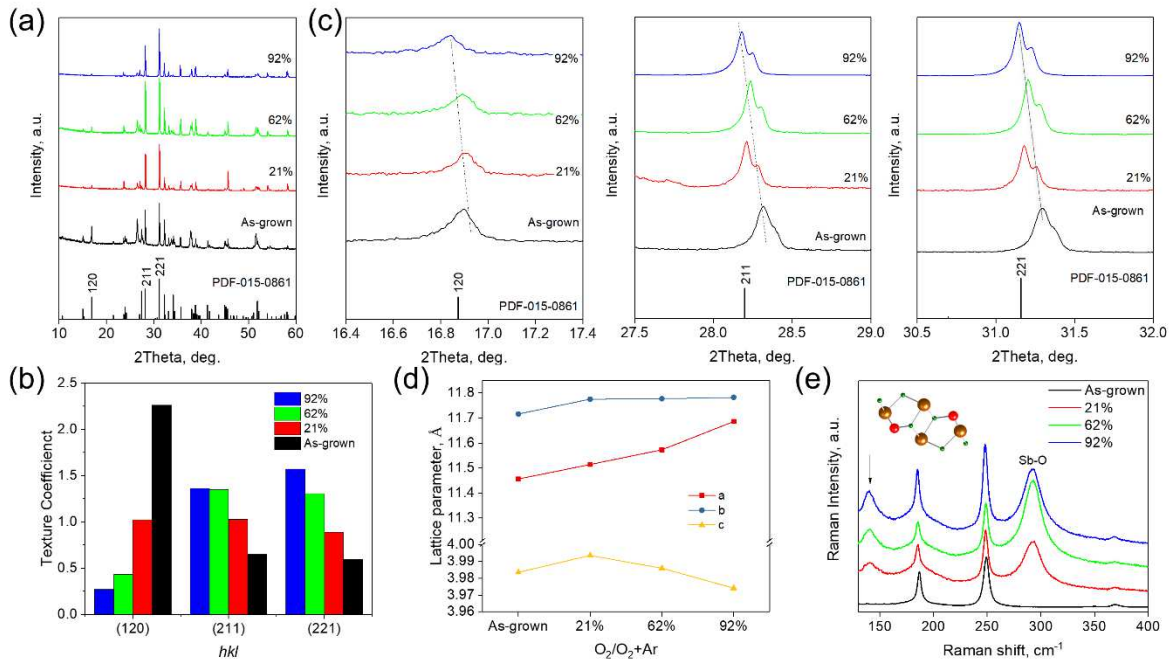

Fig 3. Characterization of Sb_2Se_3 films grown on the oxygenated CBD CdS buffer layer. (a) X-ray diffraction (XRD) spectra of the Sb_2Se_3 films. (b) The texture coefficient for the selected peaks, (c) XRD spectra shift to lower angle in (120), (211) and (221) peaks, (d) the lattice parameters for the Sb_2Se_3 film and (e) Raman spectra of the Sb_2Se_3 film. The inset of (e) shows oxygen form the bond between Sb and Se to generate the –Sb-O-Se- chain.

The 800 nm thick Sb_2Se_3 films were grown on the oxygenated CBD CdS:O substrates using the close-spaced sublimation (CSS).[43] The XRD spectra of the Sb_2Se_3 films (Fig.3a) show high crystallinity. The observed XRD spectra agree well with the PDF-015-0861 with orthorhombic space group (Pnma, No. 62). The calculated texture coefficients (TCs) of diffraction peaks of the samples are shown in Fig. 3b, where a large TC value suggests a preferred orientation of the grains in the films[5]. It shows that the oxygen in CdS could significantly impact the Sb_2Se_3 orientation, for example, the $TC_{(120)}$ is reduced with increasing oxygen concentration, while the $TC_{(211)}$ and $TC_{(221)}$ are gradually enhanced with increasing oxygen concentration. The preferred (211) and (221) orientations with the increased oxygen concentration in CdS:O suggest that the orientation of $(Sb_4Se_6)_n$ ribbon could be tuned via the oxygen diffusion from the buffer layer to the absorber.

To investigate the impact of oxygenated CdS window layer on the growth behavior of the Sb_2Se_3 film, the selected (120), (211) and (221) peaks are zoomed in and shown in Fig. 3c, lattice expansion can be observed with the peak position shifted to the lower angle side when oxygen concentration increases. The calculated lattice parameters with the orthorhombic structure are shown in Fig. 3d. The *a*-axis lattice parameter increases from 11.4 to 11.8 Å (~2 % increase) with increasing oxygen concentration in the CBD CdS buffer layer, while the *b* and *c* lattice parameters remain almost constantly (less than 0.5% variation). This is evidence that the oxygen diffuses from the oxygenated CdS to Sb_2Se_3, and the *a*-axis expands while *c* axis decreases slightly. The distribution of oxygen atoms in the Sb_2Se_3 may be dominated by the interstitial sites instead of substitutional on the Se sites. Otherwise, the substitution of oxygen on the Se sites should reduce the lattice parameters due to the smaller oxygen ion radius. In the case of the oxygen interstitials in Sb_2Se_3, the possible site is the vdWs gap between the $(Sb_4Se_6)_n$ ribbons in the [100] and [010] directions without dangling bonds[6]. This suggests that the oxygen in the vdW gap prefers the interstitial site that bonds to Sb/Se since the inter-chain between Se-Sb is weak[44]. The oxygen bond may be associated with the bridged ring with the stoichiometry $SbSeO_x$, as shown in the inset of Fig. 3e. The closed ring with -Sb-O-Se- chain could significantly impact the bond energy and bond length due to the introduced chemical strain. The Raman spectra with the oxygenated CdS windows layers was shown in Fig. 3e. The Sb-O bonds (i.e., 291 cm^{-1}) appear in the Sb_2Se_3 film with oxygenated CdS windows layers compared to the as-grown CdS windows layer. In addition, it is notable that a new mode located at ~ 140 cm^{-1} appears in Sb_2Se_3 deposited on the oxygenated CdS windows layers. This is in agreement with the Raman D1 mode at 3.6 GPa reported in high-pressure Raman scatting study on Sb_2Se_3[45]. Meanwhile, the large lattice mismatch between the wurtzite CdS and orthorhombic Sb_2Se_3 could be reduced with Sb-O-Se bridging at the

CdS:O/Sb_2Se_3 interface, which may suppress the carrier recombination at the heterojunction interface. The distribution of oxygen in the Sb_2Se_3 vdW gap could also boost the carrier transport since the $(Sb_4Se_6)_n$ ribbons are tuned to the preferred direction, that is, normal to the substrate [6] (as shown in Fig. 3b). These observations are also in agreement with our theoretical calculation above.

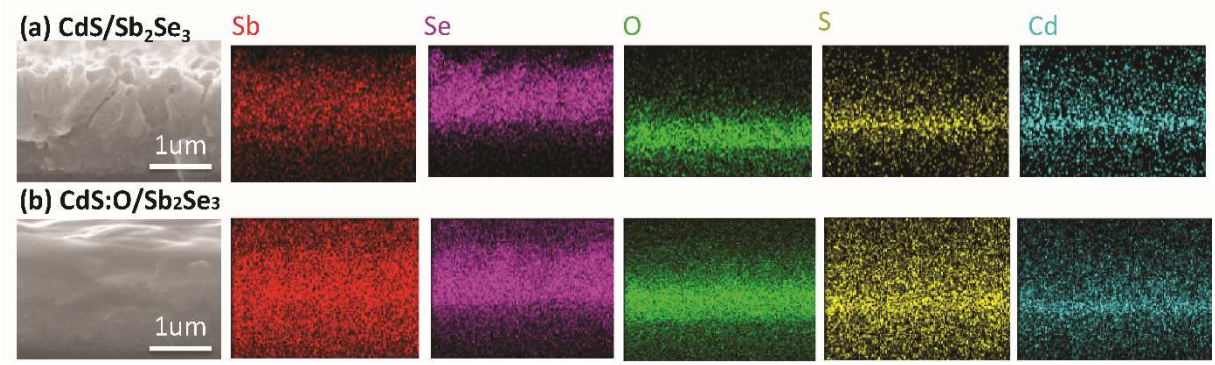

Fig. 4 Cross-sectional SEM and EDS elemental mapping for (a) CdS/Sb_2Se_3 and (b) 91% O/Ar+O annealed CdS:O/Sb_2Se_3 thin film.

To ascertain about the oxygen distribution in the interfacial area, scanning electron microscopy (SEM) cross-sectional analysis and corresponding EDS elemental mapping was conducted, as shown in Fig. 4. The elemental distribution of Sb and Se are uniform and in a desired 2:3 ratio, and Cd/S ratios are about 1, indicating that the Sb_2Se_3/CdS heterostructure is formed. However, the oxygen distribution (here, the oxygen from the FTO also collected) are increased in the oxygenated CdS:O/Sb_2Se_3 (Fig. 4b) compared to that of CdS/Sb_2Se_3 (Fig. 4a). The oxygen in the CdS:O/ Sb_2Se_3 interface can also be diffused into the Sb_2Se_3 absorber layer.

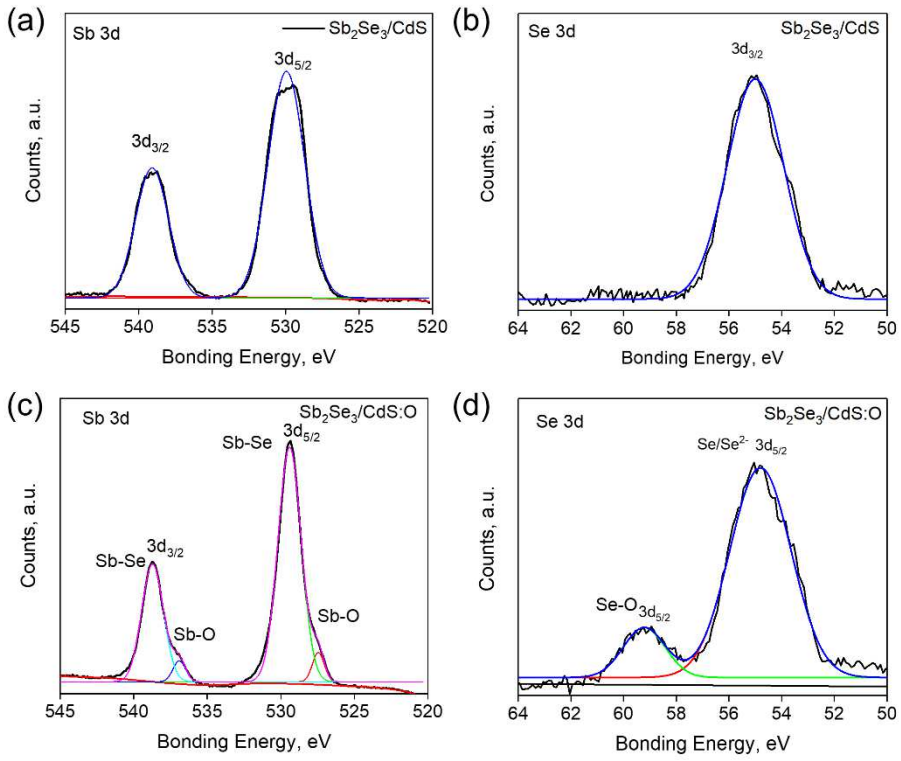

Fig. 5. XPS of Sb_2Se_3 film with oxygenated CBD CdS. Sb 3d with (a) CdS and (c) CdS:O buffer layer and XPS of Se 3d with (b) CdS and (d) CdS:O buffer layer.

To ascertain about the oxygen sites in the Sb_2Se_3 absorber with CdS:O window layer, X-ray photoelectron spectroscopy (XPS) was employed to determine the bonding states. To prevent the surficial oxygen impact, we do Ar ions etching for the top layer 20 nm of the Sb_2Se_3 before measuring the XPS. As shown in Fig. 5a, the Sb 3d peaks can be observed in the as-grown Sb_2Se_3 films with as grown CdS windows layer, corresponding to the Sb $3d_{3/2}$, and $3d_{5/2}$, respectively. However, with the oxygenated CBD CdS:O buffer layer, two pairs of Sb 3d peaks were found with strong and weak peaks associated with Sb-Se and Sb-O bond, respectively, indicating oxygen diffuses from the oxygenated CdS buffer layer into the Sb_2Se_3 absorber layer. Meanwhile, Fig. 4b and 4d show the Se 3d spectra with CdS and CdS:O buffer layer, respectively. It is shown that the Se-O bond is formed in the oxygenated CdS buffer layer (Fig. 5d), suggesting that the oxygen diffused from the CdS:O layer also form bonds with the Se ions. It may form Sb-O-Se chains or

$SbSeO_x$ compounds in Sb_2Se_3 film, consistent with the tentatively proposed crystal structures by first-principles calculations in Fig. 1a and 1b.

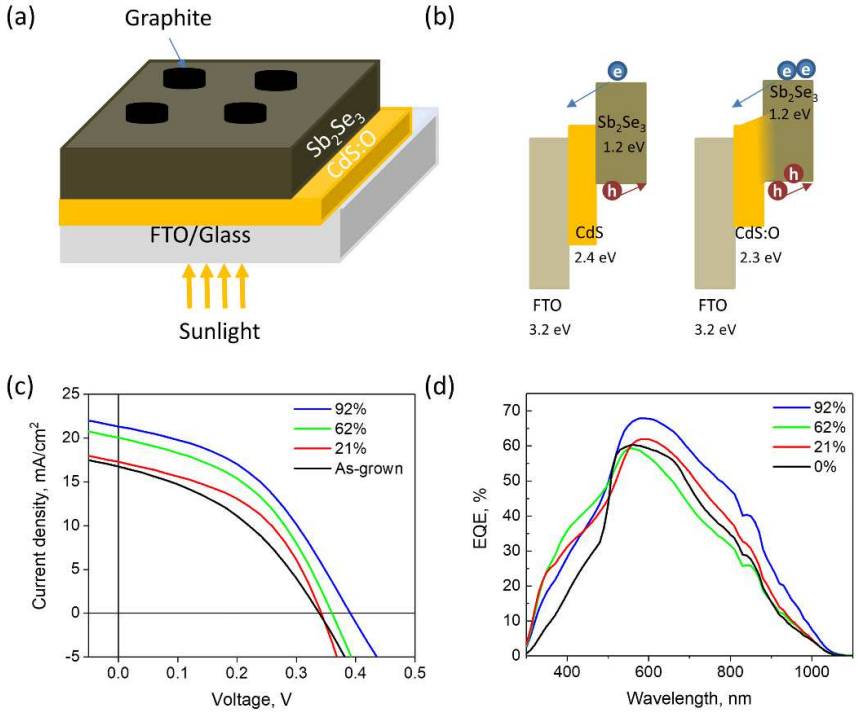

Fig. 6. Sb_2Se_3 solar cell device performance with the oxygenated CdS buffer layer. (a) Current density-voltage (*J-V*) curves and (b) external quantum efficiency (EQE) spectra of the Sb_2Se_3 solar cells on oxygenated CdS films.

Table 1. Device parameters of glass/TCO/CdS:O/Sb_2Se_3/graphite solar cell devices

O_2% in CdS:O	V_{oc}, V	J_{sc}, mA/cm^2	Fill Factor, FF, %	PCE, %	R_s, Ω cm^2	R_{sh}, Ω cm^2
As-grown	0.338	16.71	39.3	2.2	114.8	799.8
21%	0.341	17.28	45.9	2.70	73.6	946.5
62%	0.360	20.01	44.3	3.19	83.8	889.8
92%	0.391	21.32	43.1	3.59	108.1	1016.1

Figure 5a illustrates the cell structure with the oxygenated CBD CdS buffer layer and the graphite top electrode. As shown in Fig. 6b, the band alignment among CdS, oxygenated CdS:O and Sb_2Se_3 leads to the electron-hole pair dissociation and charge transfer at the interface. With

the introduction of oxygen at the interface of CdS/Sb_2Se_3 and the oxygen-filled vdW gap in the Sb_2Se_3, the heterostructure interface quality is improved, and gradient bandgap may be formed due to the consumption of the oxygen. The oxygen inside the Sb_2Se_3 vdW gaps may assist in carrier transport. Thus, higher device performance is expected in the oxygenated CdS buffer layer. Figure 6c shows the *J-V* curves of typical Sb_2Se_3 solar cells in the configuration FTO/CdS:O/Sb_2Se_3/graphite/Ag. The corresponding device parameters are given in Table 1. The oxygenated CdS in 92% oxygen partial pressure achieved the best devices perform as expected with PCE of 3.59%, V_{oc} of ~ 0.391 V, and J_{sc} of 21.32 mA cm^{-2}. Here the improved V_{oc} and J_{sc} could be attributed to the tilted $(Sb_4Se_6)_n$ ribbons normal to the substrate as proved previously through the texture coefficient analysis, and also origin from the suppressed interface recombination. The series resistivity (R_{oc}) and shunt resistivity (R_{sh}) show slight improvement with increasing oxygen concentration, which is in good agreement with other oxygenated CdS buffered solar cells due to the improved resistivity of oxygenated CdS layer[20]. The other potential reason for the improved resistivity may be ascribed to the Sb_2Se_3 absorber layer with more oxygen[14]. As shown in Figure 6d, the external quantum efficiency (EQE) curves of these CdS:O/Sb_2Se_3 cells demonstrate an enhanced photoabsorption in the short (< 500 nm) and long (>700) wavelength regions, indicating the improved current collection in these two regions and contribute to the improve photocurrent. In addition, the EQE maxima shift from ~2.3 to ~2.1 eV with increasing oxygen partial pressure, confirming a redshift associated with the decreased bandgap of CdS:O buffer layers, which is in agreement with our previous UV-Vis optical measurement.

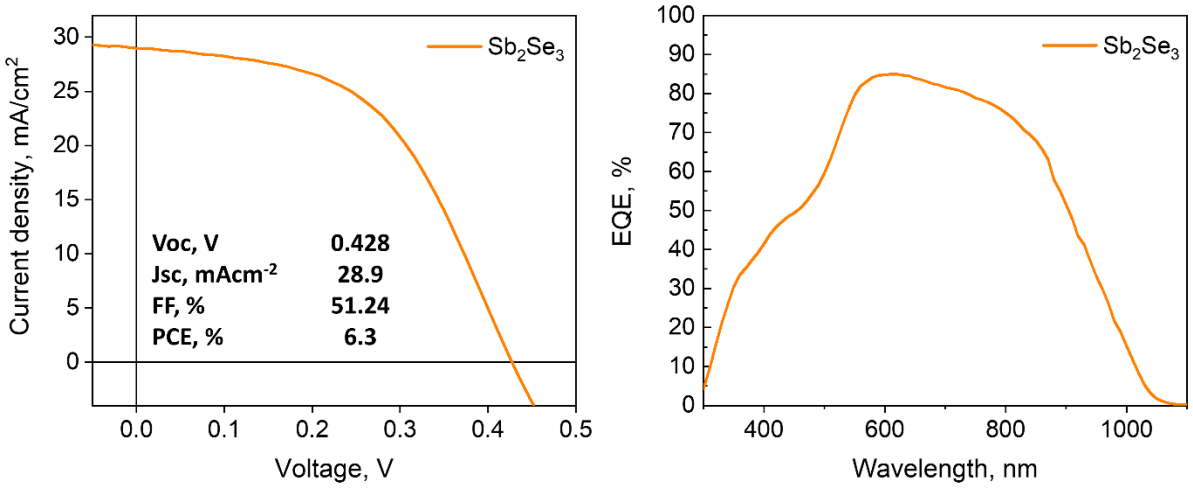

Fig. 7. Sb_2Se_3 solar cell champion device with the optimized oxygenated CdS buffer layer. (a) Current density-voltage (*J-V*) curves and (b) external quantum efficiency (EQE) spectra of the Sb_2Se_3 solar cells on oxygenated CBD CdS films.

With the optimization of the oxygenated CBD CdS window layer thickness (~ □□□nm), Sb_2Se_3 CSS growth conditions and thickness (~ 1 □m) (e.g., tuning the growth rate), and reduce the graphite electrode resistivity, we achieved a champion solar cells with V_{oc} 0.428V, J_{sc} of 28.9 $mAcm^{-2}$, and Fill factor (*FF)* of 51.24% and a PCE of 6.3% (as shown in Fig. 6a). The device optimization process can be found elsewhere. [43] This is among the highest efficiencies so far for Sb_2Se_3 solar cells with graphite back contact. Here the low *FF* compared to the reported high-efficiency Sb_2Se_3 solar cells may be ascribed to the higher series resistivity of the graphite electrode and interface between Sb_2Se_3/graphite than that cells with thin Au electrode.[5, 11] The EQE response for the champion devices was shown in Fig. 6b. An EQE of 85% can be achieved at a wavelength of 604 nm, which is on par with the previously reported high-efficiency Sb_2Se_3 devices, slightly lower due to the lack of the hole transport layer, such as PbS, spiro-OMeTAD.[4, 12]

4. Conclusion

In summary, the interface engineering of the oxygenated CBD CdS buffer layer has been employed to tailor the Sb_2Se_3 solar cells to achieve high PCE ~6.3%. The study of native and extrinsic defects in the absorber layer, the fundamental structural and electronic properties of Sb-$_2$Se$_3$ with potential O-doped defects, the interface engineering improved microstructure, and electronic structure in the oxygenated CBD CdS have been systematically investigated using both theoretical and experimental methods. The Sb_2Se_3 films show gradual lattice expansion in *a*-axis/[001] direction, suggesting that the oxygen diffuses from oxygenated CdS buffer layer to the interstitial sites in the van der Waals gap of the inter-Sb_2Se_3 ribbons, stabilized by the formation of Sb-O-Se chain. The $(Sb_4Se_6)_n$ ribbons are also found to be normal to the substrate with increasing oxygen in the CdS:O buffer due to the preference of forming Sb-O-Se chains. This work demonstrates that the optimized buffer/Sb_2Se_3 interface and oxygen in Sb_2Se_3 could provide a unique pathway to tailor the optical and electronic behavior and improve the efficiency of non-cubic chalcogenide solar cells.

Acknowledgments

L.G. and B.Z. contribute equally to the paper. The authors gratefully acknowledge the startup fund from the University of Alabama. B.Z. and X.Q. acknowledge the startup fund of Texas A&M University.

References

[1] A. Polman, M. Knight, E.C. Garnett, B. Ehrler, W.C. Sinke, Photovoltaic materials: Present efficiencies and future challenges, Science 352(6283) (2016).

[2] S. Chu, Y. Cui, N. Liu, The path towards sustainable energy, Nature Mater. 16 (2016) 16.

[3] M.A. Green, S.P. Bremner, Energy conversion approaches and materials for high-efficiency photovoltaics, Nature Mater. 16 (2016) 23.

[4] C. Chen, L. Wang, L. Gao, D. Nam, D.B. Li, K.H. Li, Y. Zhao, C. Ge, H. Cheong, H. Liu, H.S. Song, J. Tang, 6.5% Certified Efficiency Sb2Se3 Solar Cells Using PbS Colloidal Quantum Dot Film as Hole-Transporting Layer, Acs Energy Lett 2(9) (2017) 2125-2132.

[5] L. Wang, D.B. Li, K.H. Li, C. Chen, H.X. Deng, L. Gao, Y. Zhao, F. Jiang, L.Y. Li, F. Huang, Y.S. He, H.S. Song, G.D. Niu, J. Tang, Stable 6%-efficient Sb2Se3 solar cells with a ZnO buffer layer, Nat Energy 2(4) (2017).

[6] Y. Zhou, L. Wang, S. Chen, S. Qin, X. Liu, J. Chen, D.-J. Xue, M. Luo, Y. Cao, Y. Cheng, E.H. Sargent, J. Tang, Thin-film Sb2Se3 photovoltaics with oriented one-dimensional ribbons and benign grain boundaries, Nature Photonics 9 (2015) 409.

[7] Z. Li, X. Liang, G. Li, H. Liu, H. Zhang, J. Guo, J. Chen, K. Shen, X. San, W. Yu, R. E. I. Schropp, Y. Mai, 9.2%-efficient core-shell structured antimony selenide nanorod array solar cell, Nature Communications, 10, 125, 2019.

[8] D. Perez-Martinez, J.D. Gonzaga-Sanchez, F. De Bray-Sanchez, G. Vazquez-Garcia, J. Escorcia-Garcia, M.T.S. Nair, P.K. Nair, Simple solar cells of 3.5% efficiency with antimony sulfide-selenide thin films, Phys Status Solidi-R 10(5) (2016) 388-396.

[9] K. Zeng, D.J. Xue, J. Tang, Antimony selenide thin-film solar cells, Semicond Sci Tech 31(6) (2016).

[10] X.Z. Wu, High-efficiency polycrystalline CdTe thin-film solar cells, Sol Energy 77(6) (2004) 803-814.

[11] C.C. Yuan, L.J. Zhang, W.F. Liu, C.F. Zhu, Rapid thermal process to fabricate Sb2Se3 thin film for solar cell application, Sol Energy 137 (2016) 256-260.

[12] D.B. Li, X.X. Yin, C.R. Grice, L. Guan, Z.N. Song, C.L. Wang, C. Chen, K.H. Li, A.J. Cimaroli, R.A. Awni, D.W. Zhao, H.S. Song, W.H. Tang, Y.F. Yan, J. Tang, Stable and efficient CdS/Sb2Se3 solar cells prepared by scalable close space sublimation, Nano Energy 49 (2018) 346-353.

[13] X. Wen, C. Chen, S. Lu, K. Li, R. Kondrotas, Y. Zhao, W. Chen, L. Gao, C. Wang, J. Zhang, G. Niu, J. Tang, Vapor transport deposition of antimony selenide thin film solar cells with 7.6% efficiency, Nat Commun 9(1) (2018) 2179.

[14] C. Chen, Y. Zhao, S. Lu, K. Li, Y. Li, B. Yang, W. Chen, L. Wang, D. Li, H. Deng, F. Yi, J. Tang, Accelerated Optimization of TiO2/Sb_2Se_3 Thin Film Solar Cells by High-Throughput Combinatorial Approach, Advanced Energy Materials 7(20) (2017) 1700866.

[15] X. Wen, Y. He, C. Chen, X. Liu, L. wang, B. Yang, M. Leng, H. Song, K. Zeng, D. Li, K. Li, L. Gao, J. Tang, Magnetron sputtered ZnO buffer layer for Sb2Se3 thin film solar cells, Solar Energy Materials and Solar Cells 172 (2017) 74-81.

[16] M. Leng, M. Luo, C. Chen, S. Qin, J. Chen, J. Zhong, J. Tang, Selenization of Sb2Se3 absorber layer: An efficient step to improve device performance of CdS/Sb2Se3 solar cells, Applied Physics Letters 105(8) (2014) 083905.

[17] J.M. Kephart, R. Geisthardt, W.S. Sampath, Sputtered, oxygenated CdS window layers for higher current in CdS/CdTe thin film solar cells, 2012 38th IEEE Photovoltaic Specialists Conference, 2012, pp. 000854-000858.

[18] N.R. Paudel, C.R. Grice, C. Xiao, Y. Yan, The effects of high-temperature processing on the structural and optical properties of oxygenated CdS window layers in CdTe solar cells, Journal of Applied Physics 116(4) (2014) 044506.

[19] D.M. Meysing, C.A. Wolden, M.M. Griffith, H. Mahabaduge, J. Pankow, M.O. Reese, J.M. Burst, W.L. Rance, T.M. Barnes, Properties of reactively sputtered oxygenated cadmium sulfide (CdS:O) and their impact on CdTe solar cell performance, J Vac Sci Technol A 33(2) (2015).

[20] J. Ge, P. Koirala, C.R. Grice, P.J. Roland, Y. Yu, X.X. Tan, R.J. Ellingson, R.W. Collins, Y.F. Yan, Oxygenated CdS Buffer Layers Enabling High Open-Circuit Voltages in Earth-Abundant Cu2BaSnS4 Thin-Film Solar Cells, Adv Energy Mater 7(6) (2017).

[21] M.M. Junda, C.R. Grice, I. Subedi, Y.F. Yan, N.J. Podraza, Effects of oxygen partial pressure, deposition temperature, and annealing on the optical response of CdS:O thin films as studied by spectroscopic ellipsometry, J Appl Phys 120(1) (2016).

[22] Y. Zhou, Y. Li, J.J. Luo, D.B. Li, X.S. Liu, C. Chen, H.B. Song, J.Y. Ma, D.J. Xue, B. Yang, J. Tang, Buried homojunction in CdS/Sb2Se3 thin film photovoltaics generated by interfacial diffusion, Appl Phys Lett 111(1) (2017).

[23] N.R. Paudel, Y. Yan, Enhancing the photo-currents of CdTe thin-film solar cells in both short and long wavelength regions, Applied Physics Letters 105(18) (2014) 183510.

[24] J.D. Poplawsky, W. Guo, N. Paudel, A. Ng, K. More, D. Leonard, Y. Yan, Structural and compositional dependence of the CdTexSe1−x alloy layer photoactivity in CdTe-based solar cells, Nature Communications 7 (2016) 12537.

[25] H. Metin, R. Esen, Annealing studies on CBD grown CdS thin films, Journal of Crystal Growth 258(1) (2003) 141-148.

[26] L. Wang, M. Luo, S.K. Qin, X.S. Liu, J. Chen, B. Yang, M.Y. Leng, D.J. Xue, Y. Zhou, L. Gao, H.S. Song, J. Tang, Ambient CdCl2 treatment on CdS buffer layer for improved performance of Sb2Se3 thin film photovoltaics, Appl Phys Lett 107(14) (2015).

[27] P. Hohenberg, W. Kohn, Inhomogeneous Electron Gas, Physical Review 136(3B) (1964) B864-B871.

[28] G. Kresse, J. Furthmüller, Efficient iterative schemes for ab initio total-energy calculations using a plane-wave basis set, Phys Rev B 54(16) (1996) 11169-11186.

[29] J.P. Perdew, K. Burke, M. Ernzerhof, Generalized Gradient Approximation Made Simple, Phys Rev Lett 77(18) (1996) 3865-3868.

[30] D.C. Langreth, M.J. Mehl, Beyond the local-density approximation in calculations of ground-state electronic properties, Phys Rev B 28(4) (1983) 1809-1834.

[31] J. Klimeš, D.R. Bowler, A. Michaelides, Van der Waals density functionals applied to solids, Phys Rev B 83(19) (2011) 195131.

[32] H.J. Monkhorst, J.D. Pack, Special points for Brillouin-zone integrations, Phys Rev B 13(12) (1976) 5188-5192.

[33] A.D. Becke, E.R. Johnson, A simple effective potential for exchange, The Journal of Chemical Physics 124(22) (2006) 221101.

[34] A.V. Krukau, O.A. Vydrov, A.F. Izmaylov, G.E. Scuseria, Influence of the exchange screening parameter on the performance of screened hybrid functionals, The Journal of Chemical Physics 125(22) (2006) 224106.

[35] L. Guo, B. Zhang, Y. Qin, D. Li, L. Li, X. Qian, F. Yan, Tunable Quasi-One-Dimensional Ribbon Enhanced Light Absorption in Sb2Se3 Thin-film Solar Cells Grown by Close-Space Sublimation, Solar RRL 2(10) (2018) 1800128.

[36] W. Kohn, L.J. Sham, Self-Consistent Equations Including Exchange and Correlation Effects, Phys. Rev. 140(4A) (1965) A1133-A1138.

[37] X. Liu, X. Xiao, Y. Yang, D.-J. Xue, D.-B. Li, C. Chen, S. Lu, L. Gao, Y. He, M.C. Beard, G. Wang, S. Chen, J. Tang, Enhanced Sb2Se3 solar cell performance through theory-guided defect control, Progress in Photovoltaics: Research and Applications 25(10) (2017) 861-870.

[38] C.Y. Moon, S.H. Wei, Y.Z. Zhu, G.D. Chen, Band-gap bowing coefficients in large size-mismatched II-VI alloys: first-principles calculations, Phys Rev B 74(23) (2006).

[39] D.A. Duncan, J.M. Kephart, K. Horsley, M. Blum, M. Mezher, L. Weinhardt, M. Häming, R.G. Wilks, T. Hofmann, W. Yang, M. Bär, W.S. Sampath, C. Heske, Characterization of Sulfur Bonding in CdS:O Buffer Layers for CdTe-based Thin-Film Solar Cells, ACS Applied Materials & Interfaces 7(30) (2015) 16382-16386.

[40] P. Parayanthal, F.H. Pollak, Raman Scattering in Alloy Semiconductors: "Spatial Correlation" Model, Phys. Rev. Lett. 52(20) (1984) 1822-1825.

[41] T. Karabacak, Y.P. Zhao, G.C. Wang, T.M. Lu, Growth-front roughening in amorphous silicon films by sputtering, Phys. Rev. B 64(8) (2001) 085323.

[42] A. Panin, A. Shugurov, Smoothening of thin film surfaces, Proceedings KORUS 2000. The 4th Korea-Russia International Symposium On Science and Technology, 2000, pp. 209-214 vol. 3.

[43] L. Guo, B. Zhang, Y. Qin, D. Li, L. Li, X. Qian, F. Yan, Tunable Quasi-One-Dimensional Ribbon Enhanced Light Absorption in Sb2Se3 Thin-film Solar Cells Grown by Close-Space Sublimation, Solar RRL 0(0) (2018) 1800128.

[44] V.L. Deringer, R.P. Stoffel, M. Wuttig, R. Dronskowski, Vibrational properties and bonding nature of Sb2Se3 and their implications for chalcogenide materials, Chemical Science 6(9) (2015) 5255-5262.

[45] I. Efthimiopoulos, J.M. Zhang, M. Kucway, C. Park, R.C. Ewing, Y.J. Wang, Sb2Se3 under pressure, Scientific Reports 3 (2013) 2665

Supporting Information

Interfacial engineering of oxygenated chemical bath-deposited CdS window layer for highly efficient Sb_2Se_3 thin-film solar cells

Liping Guo[a,1], Baiyu Zhang[b,1], Shan Li[c], Lin Li[a], Guozhong Xing[d], Qian Zhang[c*], Xiaofeng Qian[b**] and Feng Yan[a,e***]

[a]Department of Metallurgical and Materials Engineering, The University of Alabama, Tuscaloosa, Alabama, 35487, USA
[b]Department of Materials Science and Engineering, College of Engineering and College of Science, Texas A&M University, College Station, Texas 77843, USA
[c]Department of Materials Science and Engineering, Harbin University of Technology, Shenzhen, 518055, China.
[d]United Microelect Corp. Ltd., 3 Pasir Ris Dr 12, Singapore 519528, Singapore
[e]Center for Materials in Information Technology, The University of Alabama, Tuscaloosa, AL, 35487

[1]These authors contribute equally to the paper.

[*] corresponding author email: zhangqf@hit.edu.cn
[**] corresponding author email: feng@tamu.edu
[***] corresponding author email: fyan@eng.ua.edu

1. Computational Methods

Atomistic, electronic structures, and defect formation energy were calculated using first-principles density functional theory (DFT)[1-2] as implemented in the Vienna Ab initio Simulation Package (VASP)[3]. The Perdew-Burke-Ernzerhof (PBE)[4] form of exchange-correlation functional within the generalized gradient approximation (GGA)[5] and a plane wave basis set with a 400eV energy cutoff were employed for VASP calculations. Since van der Waals interaction is present between neighboring $(Sb_4Se_6)_n$ ribbons, we adopted the optB86-vdW non-local correlation functional that approximately accounts for dispersion interactions[6-8]. The structural optimization and electronic relaxation were calculated using a Γ-centered Monkhorst-Pack[9] k-point sampling grid of 4×4×12. The maximal residual force of each atom is less than 0.01 eV $Å^{-1}$ and the convergence criteria for electronic relaxation was set to 10^{-6} eV. As the DFT-GGA often underestimates the band gap, we adopt hybrid HSE06 functional[10] for electronic structure calculation. A k-point grid of 3×3×9 was used in the HSE06 calculations. The valence band minimum (VBM) and conduction band maximum (CBM) obtained from the DFT-HSE06 calculation were adopted to correct the defect formation energy.

The charged defect formation energy is defined as[11]

$$\Delta E^f = E(D,q) - E(bulk) - \Sigma n_i \mu_i + q\epsilon_F + E_{corr},$$

where $E(bulk)$ and $E(D,q)$ are the total energy of the host cell and the supercell with defect D in the charge state q. μ_i refers to the chemical potential of species i involved in the defect, and n_i is the number of atoms added ($n_i > 0$) or removed ($n_i < 0$). $q\epsilon_F$ represents the chemical potential of electron reservoir, *i.e.* the Fermi level. ϵ_F is conventionally referenced to the VBM in the perfect cell, and a diagram of formation energy as a function of the Fermi energy is plotted. E_{corr} stands for a correction due to the image interaction of the defect under periodic boundary condition, which aligns the electrostatic potentials in the defect supercell and the pristine bulk[12-14].

The chemical potential corresponds to the energy of exchanging atoms between the defect and the element reservoir. μ_i can be split to two parts, which is $\mu_i = \mu_i^o + \Delta\mu_i$. μ_i^o represents the chemical potential of the reference, associated with the elemental phases of each species, and $\Delta\mu_i$ is the allowed chemical potential variation. $\Delta\mu_i$ is determined by the rule that Sb_2Se_3 must be more stable than any other competing phase. Thus, in order to prevent the formation of the standard elementary phases or any competing compounds, such as antimony oxides, the chemical potential of each element should be subject to the followed constraints:

$\Delta\mu_{Sb} \leq 0,\ \Delta\mu_{Se} \leq 0,\ \Delta\mu_O \leq 0.$

$3\Delta\mu_{Se} + 2\Delta\mu_{Sb} \leq \Delta E_f(Sb_2Se_3) = -1.33\ \text{eV/formula}$

$n\Delta\mu_O + m\Delta\mu_{Sb} \leq \Delta E_f(Sb_mO_n)$

$\mu_{Sb}^{o} = -4.14\ eV; \mu_{Se}^{o} = -3.48\ eV; \mu_{O}^{o} = -4.4\ eV$

$\mu_i = \mu_i^o + \Delta\mu_i$

There are three possible antimony oxides, Sb_2O_3, SbO_2, and Sb_2O_5. The chemical potential of each element is associated with the synthesis conditions. In the calculation, we consider two extrema, that is, Se rich ($\Delta\mu_{Se} = 0$) and Se poor ($\Delta\mu_{Sb} = 0$), and the allowed oxygen chemical potential is shown in Fig. 1(c).

μ_i	Sb poor ($\Delta\mu_{Se} = 0$)	Sb rich ($\Delta\mu_{Sb} = 0$)
Sb	-4.81 eV	-4.14 eV
Se	-3.48 eV	-3.92 eV
O	-6.90 eV	-7.35 eV

Table S1. Chemical potential of atomic species.

2. Crystal Structures

Lattice Constants (Å)	ICSD	GGA	GGA + vdW
a	11.648	4.030	11.482
b	11.794	12.843	11.870
c	3.986	4.030	4.014

Table S2. Calculated and experimental lattice parameters. Experimental values were obtained from the Inorganic Crystal Structure Database (ICSD).

3. Electronic Structure

To investigate the impact of defects on the electronic structure, we plot the band structures of Sb_2Se_3 crystal with and without defects. When Se vacancy is present in the crystal, a flat band appears in the middle of the band gap, known as defect localized state (DLS). DLSs can serve as the recombination center and decrease the carrier concentrations. On the contrary, there is no DLS state in the oxygen doped cells. The band structures shown below confirm the results of defect study, where the transition level is above the CBM in the presence of O interstitials.

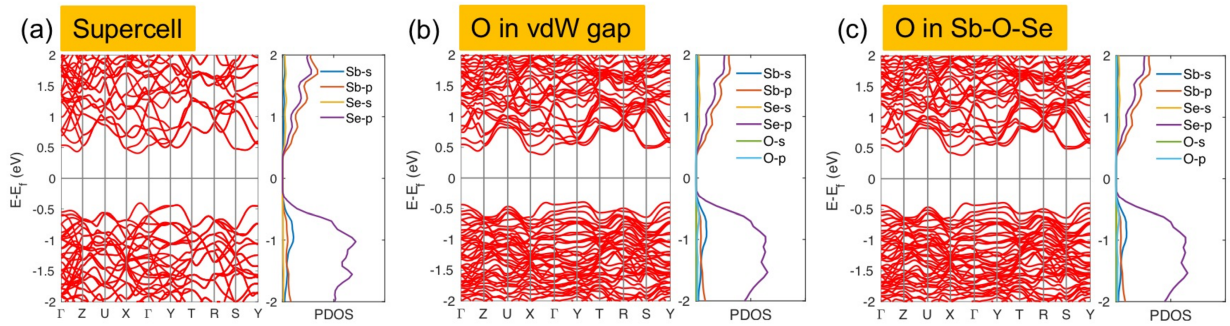

Figure S1. Calculated band structures of Sb_2Se_3 host cell with and without defects associated with oxygen sites.

4. Experimental Results

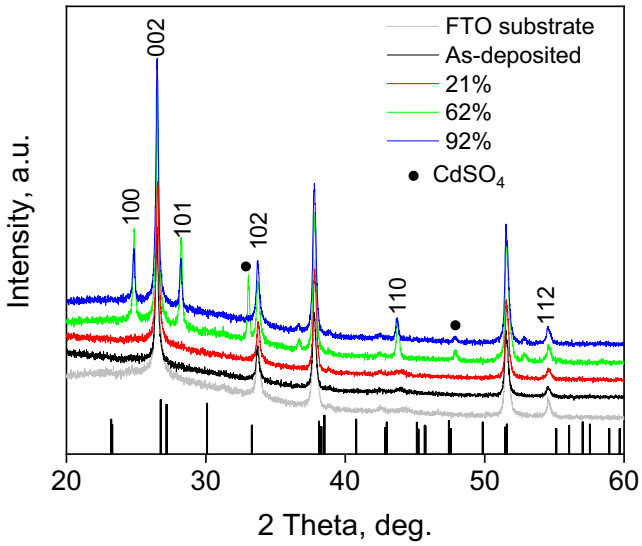

Figure S2. X-ray spectra with the $CdSO_4$ phase in the oxygenated CBD CdS film at higher oxygen annealing atmosphere.

References:

(1) Kohn, W.; Sham, L. J. Self-Consistent Equations Including Exchange and Correlation Effects. *Physical Review* **1965,** *140* (4A), A1133-A1138, DOI: 10.1103/PhysRev.140.A1133.

(2) Hohenberg, P.; Kohn, W. Inhomogeneous Electron Gas. *Physical Review* **1964,** *136* (3B), B864-B871, DOI: 10.1103/PhysRev.136.B864.

(3) Kresse, G.; Furthmüller, J. Efficient iterative schemes for ab initio total-energy calculations using a plane-wave basis set. *Phys Rev B* **1996,** *54* (16), 11169-11186, DOI: 10.1103/PhysRevB.54.11169.

(4) Perdew, J. P.; Burke, K.; Ernzerhof, M. Generalized Gradient Approximation Made Simple. *Physical Review Letters* **1996,** *77* (18), 3865-3868.

(5) Langreth, D. C.; Mehl, M. J. Beyond the local-density approximation in calculations of ground-state electronic properties. *Phys Rev B* **1983,** *28* (4), 1809-1834, DOI: 10.1103/PhysRevB.28.1809.

(6) Klimeš, J.; Bowler, D. R.; Michaelides, A. Van der Waals density functionals applied to solids. *Phys Rev B* **2011,** *83* (19), 195131, DOI: 10.1103/PhysRevB.83.195131.

(7) Dion, M.; Rydberg, H.; Schröder, E.; Langreth, D. C.; Lundqvist, B. I. Van der Waals Density Functional for General Geometries. *Physical Review Letters* **2004,** *92* (24), 246401, DOI: 10.1103/PhysRevLett.92.246401.

(8) Román-Pérez, G.; Soler, J. M. Efficient Implementation of a van der Waals Density Functional: Application to Double-Wall Carbon Nanotubes. *Physical Review Letters* **2009,** *103* (9), 096102, DOI: 10.1103/PhysRevLett.103.096102.

(9) Monkhorst, H. J.; Pack, J. D. Special points for Brillouin-zone integrations. *Phys Rev B* **1976,** *13* (12), 5188-5192, DOI: 10.1103/PhysRevB.13.5188.

(10) Influence of the exchange screening parameter on the performance of screened hybrid functionals. *The Journal of Chemical Physics* **2006,** *125* (22), 224106, DOI: 10.1063/1.2404663.

(11) Freysoldt, C.; Grabowski, B.; Hickel, T.; Neugebauer, J.; Kresse, G.; Janotti, A.; Van de Walle, C. G. First-principles calculations for point defects in solids. *Reviews of Modern Physics* **2014,** *86* (1), 253-305, DOI: 10.1103/RevModPhys.86.253.

(12) Péan, E. V.; Barreau, N.; Vidal, J.; Latouche, C.; Jobic, S. Theoretical investigation of $CdIn_2S_4$: A possible substitute for CdS in $CuIn_{1-x}Ga_xSe_2$-based photovoltaic devices. *Physical Review Materials* **2017,** *1* (6), 064605, DOI: 10.1103/PhysRevMaterials.1.064605.

(13) Broberg, D.; Medasani, B.; Zimmermann, N. E. R.; Yu, G.; Canning, A.; Haranczyk, M.; Asta, M.; Hautier, G. PyCDT: A Python toolkit for modeling point defects in semiconductors and insulators. *Computer Physics Communications* **2018,** *226*, 165-179, DOI: 10.1016/j.cpc.2018.01.004.

(14) Stephan, L.; Alex, Z. Accurate prediction of defect properties in density functional supercell calculations. *Modelling and Simulation in Materials Science and Engineering* **2009,** *17* (8), 084002.